



Synthesis of flower-like heterostructured β - $\text{Bi}_2\text{O}_3/\text{Bi}_2\text{O}_2\text{CO}_3$ microspheres using $\text{Bi}_2\text{O}_2\text{CO}_3$ self-sacrifice precursor and its visible-light-induced photocatalytic degradation of *o*-phenylphenol

Ruiping Hu, Xin Xiao*, Shunheng Tu, Xiaoxi Zuo, Junmin Nan*

School of Chemistry and Environment, South China Normal University; Guangzhou Key Laboratory of Materials for Energy Conversion and Storage, Guangzhou 510006, PR China

ARTICLE INFO

Article history:

Received 4 June 2014

Received in revised form 11 August 2014

Accepted 17 August 2014

Available online 22 August 2014

Keywords:

β - $\text{Bi}_2\text{O}_3/\text{Bi}_2\text{O}_2\text{CO}_3$ microspheres

p–n junction

o-Phenylphenol

Visible-light photocatalysis

Photodegradation mechanism

ABSTRACT

Novel flower-like heterostructured β - $\text{Bi}_2\text{O}_3/\text{Bi}_2\text{O}_2\text{CO}_3$ microspheres are synthesized by calcining a $\text{Bi}_2\text{O}_2\text{CO}_3$ self-sacrifice precursor for the visible-light photocatalytic degradation of *o*-phenylphenol (OPP, is a widely used fungicide and preservative agent). The $\text{Bi}_2\text{O}_2\text{CO}_3$ microspheres are firstly prepared under hydrothermal conditions, and then converted to Bi_2O_3 by thermal treatment. With increasing the calcining temperature from 250 to 500 °C, an in situ stepwise decomposition reaction take place during the course of calcination, described as: $\text{Bi}_2\text{O}_2\text{CO}_3 \rightarrow \beta\text{-Bi}_2\text{O}_3/\text{Bi}_2\text{O}_2\text{CO}_3 \rightarrow \beta\text{-Bi}_2\text{O}_3 \rightarrow \beta\text{-Bi}_2\text{O}_3/\alpha\text{-Bi}_2\text{O}_3 \rightarrow \alpha\text{-Bi}_2\text{O}_3$. The $\beta\text{-Bi}_2\text{O}_3/\text{Bi}_2\text{O}_2\text{CO}_3$ microspheres synthesized at 300 °C exhibit excellent photocatalytic activity under visible-light irradiation, which can degrade 99.8% OPP in 45 min. And the degradation rate of the heterostructured photocatalyst is approximately 2, 2.6, 6, 13, 80, and 827 times higher than that of single $\beta\text{-Bi}_2\text{O}_3$, mixed $\beta\text{-Bi}_2\text{O}_3$ and $\text{Bi}_2\text{O}_2\text{CO}_3$, commercial $\beta\text{-Bi}_2\text{O}_3$, $\alpha\text{-Bi}_2\text{O}_3$, N-doped TiO_2 , and $\text{Bi}_2\text{O}_2\text{CO}_3$, respectively. The superior photoreactivity of the $\beta\text{-Bi}_2\text{O}_3/\text{Bi}_2\text{O}_2\text{CO}_3$ is attributed to the enhanced charge separation and transfer due to the formation of p–n junction with large heterojunction interface, favorable band gap energy (2.27 eV), relatively high specific surface areas ($12.5 \text{ m}^2 \text{ g}^{-1}$), and flower-like hierarchical micro/nano structures. In addition, the degradation intermediates including ethyl phenethyl ether, phenyl acetaldehyde, and phenylacetic acid are identified. And the results also reveal that the photogenerated holes and $\bullet\text{O}_2^-$ radicals are primarily reactive species in the photocatalytic system, which are the key factors responsible for the nearly complete mineralization of OPP.

© 2014 Elsevier B.V. All rights reserved.

1. Introduction

o-phenylphenol ($\text{C}_{12}\text{H}_{10}\text{O}$, OPP), an important phenol chemical and widely used as fungicide and preservative agent in agriculture and industry, its residue is suspected to be a potential carcinogen that can induce disturbances in growth, decrease in fertility, and kidney damage [1]. Although the OPP contaminated systems can be recovered by the techniques such as biodegradation [2,3], physical adsorption [4], UV/ H_2O_2 degradation [5], and ozone oxidation [6], some crucial challenges including high cost, toxic by-products, and long processing time remain unsolved. Photocatalytic degradation, which can utilize sunlight as an energy source to achieve high mineralization, low toxicity, low cost, and the ability to function under ambient conditions, is a promising clean alternative technology for handling OPP in wastewaters [7]. Khodja et al. demonstrated the

photocatalytic degradation of OPP in the presence of TiO_2 and ZnO semiconductors [8], but the visible-light-induced photocatalytic degradation of OPP, especially for the photocatalytic mechanism, has rarely been reported.

The key issue for the photocatalytic degradation of phenol contaminants in wastewaters is choosing the photocatalysts. Pure TiO_2 suffers from low light utilization (<5% of the solar spectrum) and poor quantum efficiency [9], which hinders its practical application. Whereas, Bi-based compounds, such as BiOX ($\text{X} = \text{Cl}, \text{Br}, \text{I}$) [10], BiVO_4 [11], Bi_2WO_6 [12], Bi_2MoO_6 [13], $\text{Bi}_2\text{O}_2\text{CO}_3$ [14], and Bi_2O_3 [15], have shown potential application in the photocatalytic degradation of organic pollutants under visible-light irradiation due to their fresh-construction and well-dispersed valence bands by the hybridization of Bi 6s and O 2p orbitals [16]. Among the Bi-based photocatalysts, Bi_2O_3 has captured considerable attention due to its excellent properties, such as high refractive index, visible-light activity, dielectric permittivity, and marked photoluminescence properties [17,18]. Bi_2O_3 has five main crystallographic polymorphs including monoclinic α , tetragonal β , body centered

* Corresponding author. Tel.: +86 20 39310255; fax: +86 20 39310187.
E-mail address: jmnann@scnu.edu.cn (J. Nan).

cubic γ , cubic δ , and triclinic ω [19]. Bi_2O_3 is a p-type semiconductor with suitable band edge potentials for water oxidation, and the band gaps of α and β - Bi_2O_3 are approximately 2.8 and 2.4 eV, respectively [20,21]. Recently, many studies of the photocatalytic activities of α , β - Bi_2O_3 have been reported, and β - Bi_2O_3 typically exhibits better photocatalytic properties for the degradation of organic chemical pollutants due to its narrow band gap [22]. In addition, β - Bi_2O_3 -based heterojunctions, which allows photocatalyst to utilize more visible light and effectively suppresses photogenerated electron–hole recombination, have also been synthesized to improve their photoactivity. For example, Li et al. prepared β - $\text{Bi}_2\text{O}_3/\text{TiO}_2$ -NTs by embedding bismuth into TiO_2 nanotubes using pulse electrodeposition followed by annealing, and the compounds were easily activated by visible light due to the photosensitization by Bi_2O_3 [23]. And Xu et al. demonstrated a hierarchical micro/nano-architecture β - $\text{Bi}_2\text{O}_3/\text{Bi}_2\text{MoO}_6$ microspheres synthesized by a facile template-free solvothermal method, and the photocatalytic activity was substantially improved compared to neat β - Bi_2O_3 and Bi_2MoO_6 [24]. Similarly, β - $\text{Bi}_2\text{O}_3/\text{BiOCl}$ [25], β - $\text{Bi}_2\text{O}_3/\text{Bi}_2\text{WO}_6$ [26], β - $\text{Bi}_2\text{O}_3/\text{ZrO}_2$ [27], and β - $\text{Bi}_2\text{O}_3/\text{ZnO}$ [28] exhibited substantially enhanced photocatalytic activity due to the efficient separation of photoexcited electrons and holes.

On the other hand, the bismuth subcarbonate ($\text{Bi}_2\text{O}_2\text{CO}_3$), which is a typical “sillén” phase and belongs to the Aurivillius-related oxide family, is recognizing another important Bi-based photocatalyst. $\text{Bi}_2\text{O}_2\text{CO}_3$ has an intergrowth of $\text{Bi}_2\text{O}_2^{2+}$ layers and CO_3^{2-} layers with the plane of the CO_3^{2-} group orthogonal to the plane of the $\text{Bi}_2\text{O}_2^{2+}$ layer [29], and is environmentally benign material that has been widely used in medicine as well as microelectrode fields [30]. However, similar to TiO_2 , the large bandgap (~ 3.3 eV) of pure $\text{Bi}_2\text{O}_2\text{CO}_3$ restricts its application in photodegradation [31]. Nevertheless, recent studies have reported that $\text{Bi}_2\text{O}_2\text{CO}_3$ contains heterojunctions showing notable visible-light photocatalytic performances obtained by coupling $\text{Bi}_2\text{O}_2\text{CO}_3$ with other narrow-band semiconductors, such as $\text{Bi}_2\text{O}_2\text{CO}_3/\text{Bi}_2\text{S}_3$ [32], $\text{Bi}_2\text{O}_2\text{CO}_3/\text{Bi}_2\text{WO}_6$ [33], $\text{Bi}_2\text{O}_2\text{CO}_3/\text{Bi}_3\text{NbO}_7$ [34], and $\text{Fe}_3\text{O}_4/\text{Bi}_2\text{O}_2\text{CO}_3$ [35].

Furthermore, in order to improve the performances of photocatalysts, several studies have also reported the application of various p–n junction photocatalysts, such as p-BiOI/n-ZnTiO₃ [36], p-BiOI/n- $\text{Bi}_2\text{O}_2\text{CO}_3$ [37], p-CuO/n-ZnO [38], and p-CuO/n-BiVO₄ [39]. The p–n junction is an interesting and special heterostructure due to its internal electric field located at a p–n junction interface, and this p–n heterojunction structure can effectively promote the separation of photo-generated electron–hole pairs, which will further increase its photocatalytic ability. Thus, the photocatalysts with p–n junction can exhibit much higher photocatalytic activity than the single material, and they provide a valid method for preparing novel visible-light-driven photocatalysts. However, although the Bi_2O_3 is one of important p-type semiconductor, the reported β - Bi_2O_3 -based p–n junction photocatalysts are limited till now. And the fabrication of β - Bi_2O_3 -based heterojunctions with large contact surfaces by facile routes remains a challenge.

According to above mentioned properties of β - Bi_2O_3 and $\text{Bi}_2\text{O}_2\text{CO}_3$, they possess the conditions for building a p–n heterojunction, which has been recently validated by Cai et al. [40]. In this paper, flower-like heterostructured β - $\text{Bi}_2\text{O}_3/\text{Bi}_2\text{O}_2\text{CO}_3$ composites, which exhibit high photocatalytic and mineralization efficiency for the degradation of OPP under visible-light irradiation, are synthesized by controlled thermal treatment of $\text{Bi}_2\text{O}_2\text{CO}_3$ microspheres as a self-sacrifice precursor. The morphologies, heterostructure interface structures, surface area, and photoabsorption properties of the β - $\text{Bi}_2\text{O}_3/\text{Bi}_2\text{O}_2\text{CO}_3$ samples are characterized, the formation mechanism of the synthesized catalysts is discussed, and their visible-light-induced photocatalytic activities for the OPP degradation are investigated. In addition, the degradation intermediates

and photogenerated reactive species of the system are identified, and a possible photocatalytic degradation mechanism is proposed.

2. Experimental

2.1. Materials and methods

The OPP (purity: 99.9%) was purchased from JK Chemical Ltd. Bismuth nitrate pentahydrate ($\text{Bi}(\text{NO}_3)_3 \cdot 5\text{H}_2\text{O}$) and citric acid ($\text{C}_6\text{H}_8\text{O}_7$) were purchased from Tianjin Kermel Chemical Reagent Co. Ltd. Commercial β - Bi_2O_3 sub-microspheres with diameters of ca. 140 nm was bought from Aladdin Reagent Co., Ltd. All of the reagents were of analytical grade and used without further purification.

The $\text{Bi}_2\text{O}_2\text{CO}_3$ precursor was synthesized by a hydrothermal method according to previously described process [31] with some modifications as follows: 0.728 g of $\text{Bi}(\text{NO}_3)_3 \cdot 5\text{H}_2\text{O}$ was dissolved in 30 mL of a 1 mol L^{−1} HNO_3 solution. Then, 0.144 g of citric acid was added to the solution under magnetic stirring. The pH of the system was adjusted to approximately 6 using 8 mol L^{−1} NaOH. Subsequently, the white precursor suspension was transferred into a 45 mL Teflon-lined stainless autoclave and incubated in an oven at 180 °C for 24 h. The resulting precipitates were collected and separated by centrifugation and washed with distilled water and absolute ethanol several times followed by drying at 60 °C. Finally, the $\text{Bi}_2\text{O}_2\text{CO}_3$ precursor was calcined in a closed alumina crucible at different temperatures ranging from 250 to 500 °C for 2 h to obtain final catalysts.

2.2. Catalyst characterization

The phase composition and structure of the as-synthesized samples were determined using powder X-ray diffraction (XRD) with a Bruker D8 Advance X-ray diffractometer (Bruker AXS, Germany) with a Cu K α radiation source. The surface composition was analyzed using X-ray photoelectron spectroscopy (XPS, Kratos Axis Ultra DLD). The morphologies were characterized by scanning electron microscopy (SEM, JSM-6380-LA, JEOL, Japan) and field emission transmission electron microscopy (TEM, Tecnai G2 F20, FEI). The differential scanning calorimetric (DSC) analysis was carried out using TA DSC Q2000 at a heating rate of 10 °C min^{−1} in nitrogen atmosphere. The specific surface areas of the samples were measured by nitrogen adsorption–desorption isotherms at 77 K according to the Brunauer–Emmett–Teller analysis (BET, ASAP 2020, Micromeritics, USA). A desorption isotherm was used to determine the pore size distribution using the Barrett–Joyner–Halenda (BJH) method. The UV–vis diffuse reflection spectra (DRS) were recorded on a UV–vis spectrophotometer (UV-3010, Hitachi, Japan) using BaSO_4 as a reference and converted from reflection to absorbance by the Kubelka–Munk method. Photocurrent measurement was carried out with a CHI 660C electrochemical station (Chenhua Instruments Co. Shanghai, China) in a standard three-electrode configuration with as-prepared samples as the working electrodes, a platinum plate as the counter electrode, and a commercial Ag/AgCl electrode as the reference electrode. The electrolyte used was a 0.5 mol L^{−1} Na_2SO_4 aqueous solution. A 300 W xenon lamp (PLS-SXE300/300UV) assembled with a UV light cut off filter ($\lambda > 420$ nm) was used as the visible-light irradiation source.

2.3. Photocatalytic activity measurements

The photocatalytic degradation experiments were carried out in a photochemical reactor (XPA-VII, Nanjing Xujiang Machine-electronic Plant, China) that was equipped with a 1000 W Xe lamp

combined with a 420 nm cut-off filter as the light source. In each experiment, a certain amount of the as-synthesized catalyst (varying from 0.2 to 2.0 g L⁻¹, typically 1 g L⁻¹) was added to a 50 mL reaction solution containing OPP with various initial concentrations (ranging from 10 to 50 mg L⁻¹, typically 20 mg L⁻¹). Prior to the irradiation, the solution with the catalyst was stirred for 1 h in the dark to allow the system to reach adsorption equilibrium. During the photocatalytic process, approximately 2.5 mL of the suspension was removed at a specified time. Then, the solids were removed from the solution using a 0.45 μ m nitrocellulose filter, and the filtrate was identified using UV–vis spectroscopy (UV-1800, Shimadzu, Japan, λ = 282 nm) to obtain the OPP concentrations in the solution. The total organic carbon (TOC) concentration was measured by an automatic total organic carbon analyzer (TOC-V, Shimadzu, Japan).

2.4. Analysis of the photogenerated intermediates

The intermediates formed during the photocatalytic degradation were further analyzed by gas chromatography–mass spectrometry (GC–MS, DSQ/Trace GC Ultra, Thermo Fisher Scientific, Dreieich, Germany) using a DB 5-MS column (30 m \times 0.25 mm). After the photocatalytic reaction, the sample solutions were extracted three times with an ethyl acetate/n-hexane mixture (2:1, v/v). Then, the organic layers were collected and concentrated to approximately 1 mL using a gentle stream of high-purity nitrogen. The GC column temperature was increased from 50 to 250 °C at 5 °C min⁻¹ and maintained at 250 °C for 5 min. The injector and transfer line temperatures were 230 °C. Helium gas was used as the carrier gas at a flow rate of 1.2 mL min⁻¹. The ion MS source temperature was 250 °C, and the electron energy was 70 eV.

2.5. Quantum chemical calculation

Quantum calculation using Gaussian 09 was carried out to obtain the frontier electronic density (FED) of OPP. Hartree–Fock (HF) theory was chosen for the full optimization of geometries, and B3LYP/6-311++ G** was used as the basis set of moderate size and accuracy. All optimizations were carried out without any symmetry restrictions and were followed by harmonic frequency analyses to ensure that the optimized conformation was the true global minimum.

3. Results and discussion

3.1. Characterization of catalysts

3.1.1. Structure and composition

The chemical composition and phase structure of the as-synthesized samples were detected by XRD. As shown in Fig. 1A, all of the diffraction peaks of the precursor (prior to calcination) can be unambiguously assigned to bismuth oxide carbonate with lattice constants of $a=b=3.865$ Å and $c=13.695$ Å, which is found to match well with the standard XRD patterns for tetragonal Bi₂O₂CO₃ (JCPDS No. 41-1488). Compared with the other characteristic diffraction peaks, a significantly intense (1 1 0) diffraction peak of Bi₂O₂CO₃ phase can be seen in the XRD pattern, implying that there is a bias of orientations of the {1 1 0} crystallographic plane [31]. And the diffraction patterns remained consistent the pure Bi₂O₂CO₃ phase as the calcination temperature up to 270 °C. When the annealing temperature reached 280 °C, tetragonal β -Bi₂O₃ was generated, with lattice constants of $a=b=7.735$ Å and $c=5.628$ Å, which matched well with values from the standard

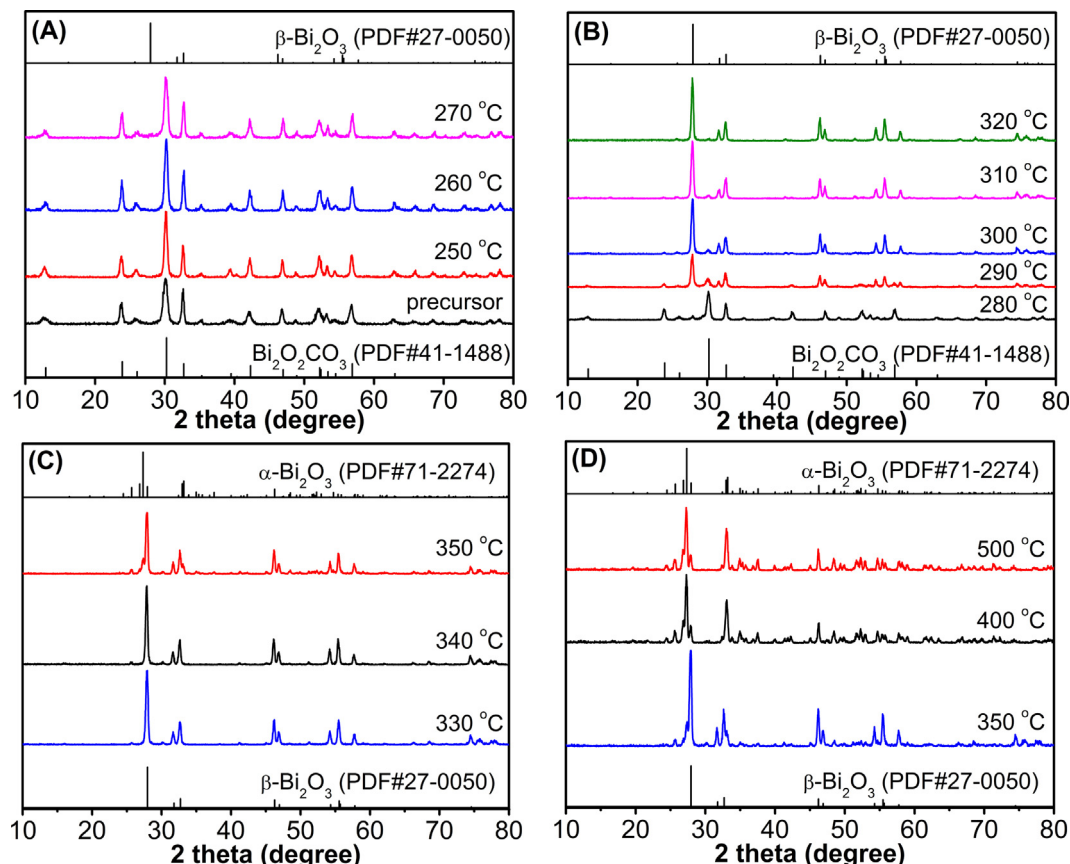


Fig. 1. XRD patterns of the samples calcined at different temperatures.

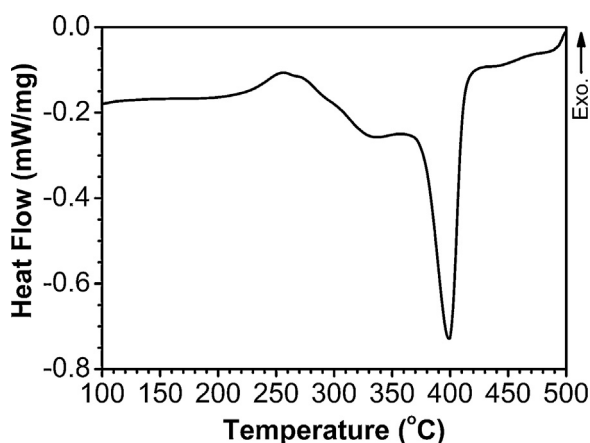
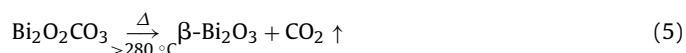
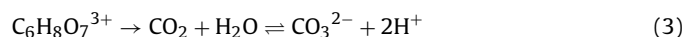


Fig. 2. DSC thermograms of the as-prepared $\text{Bi}_2\text{O}_2\text{CO}_3$ precursor.

card (JCPDS No. 27-0050). From 280 to 320 °C (Fig. 1B), the diffraction peaks of $\text{Bi}_2\text{O}_2\text{CO}_3$ in the samples gradually decreased, while the peaks of the $\beta\text{-Bi}_2\text{O}_3$ phase were simultaneously enhanced, which suggested that the formation of $\beta\text{-Bi}_2\text{O}_3/\text{Bi}_2\text{O}_2\text{CO}_3$ composites with different compositions. Highly pure $\beta\text{-Bi}_2\text{O}_3$ samples were obtained as the temperature was increased from 330 to 340 °C (Fig. 1C). If the treatment temperature was increased from 350 to 500 °C (Fig. 1D), $\beta\text{-Bi}_2\text{O}_3$ was gradually converted to monoclinic $\alpha\text{-Bi}_2\text{O}_3$ (JCPDS No. 71-2274) with lattice constants of $a = 5.857 \text{ \AA}$, $b = 8.181 \text{ \AA}$, $c = 7.515 \text{ \AA}$, and $\beta = 113.00^\circ$. And pure $\alpha\text{-Bi}_2\text{O}_3$ phase was obtained when the calcination temperature above 400 °C. It is worth mentioning that the lattice parameters show little change for each phase after the formation of $\beta\text{-Bi}_2\text{O}_3/\text{Bi}_2\text{O}_2\text{CO}_3$ or $\beta\text{-Bi}_2\text{O}_3/\alpha\text{-Bi}_2\text{O}_3$ composites, which implies that there are mixed phases in these systems rather than formation of solid solution.

In order to understand the chemical change and phase transformation during heating $\text{Bi}_2\text{O}_2\text{CO}_3$ precursor, the thermal analysis was carried out by using the DSC analysis with temperature range from room temperature to 500 °C at a heating rate of $10^\circ\text{C min}^{-1}$. It can be clearly seen from Fig. 2 that there is a broad endothermic band temperature range 270–330 °C, a strongest endothermal peak appears at 400 °C, and a relatively stable platform appears between 330 and 350 °C. The result is in agreement with the XRD analysis, i.e. tetragonal $\text{Bi}_2\text{O}_2\text{CO}_3$ is formed by a hydrothermal reaction (Eqs. (1)–(4)) [31] and converted in a stepwise fashion to $\text{Bi}_2\text{O}_2\text{CO}_3/\beta\text{-Bi}_2\text{O}_3$ and pure $\beta\text{-Bi}_2\text{O}_3$ (Eq. (5)) after thermal decomposition, then $\beta\text{-Bi}_2\text{O}_3$ transformed to $\beta\text{-Bi}_2\text{O}_3/\alpha\text{-Bi}_2\text{O}_3$ and pure $\alpha\text{-Bi}_2\text{O}_3$ (Eq. (6)) by higher temperature calcination. The chemical composition and phase structure of the synthetic samples depended on the calcination temperatures.



To further elucidate the elemental compositions and chemical states present in the as-synthesized $\beta\text{-Bi}_2\text{O}_3/\text{Bi}_2\text{O}_2\text{CO}_3$ composite, surface analysis was performed using an XPS technique for the sample annealed at 290 °C. The full survey spectrum (Fig. 3A) shows that the sample is composed of Bi, O and C elements. From Fig. 3B, the two strong peaks at 159.0 and 164.3 eV are assigned to $\text{Bi } 4f_{7/2}$ and

$\text{Bi } 4f_{5/2}$, which correspond to Bi^{3+} [41]. However, these values are not exactly the same as those obtained from pure Bi_2O_3 or $\text{Bi}_2\text{O}_2\text{CO}_3$ [42,43], which indicates that an interfacial structure is formed and the local environment and electron density of the elements change to some extent. The dominant peak of O1s (Fig. 3C) at 529.7 eV is characteristic of Bi–O bonds [42,43], and the other peaks can be assigned to CO_3^{2-} species and adsorbed surface OH^- . In addition, the core level spectrum of C1s (Fig. 3D) can be fitted with two peaks. The peak located at 284.9 eV can be assigned to adventitious carbon species from the XPS measurement [44], and the other peak located at 288.8 eV is due to the carbonate ion in $\text{Bi}_2\text{O}_2\text{CO}_3$ [29]. The results indicate the existence of Bi_2O_3 and $\text{Bi}_2\text{O}_2\text{CO}_3$, which is in good agreement with the conclusion from the XRD analysis.

3.1.2. Morphology analysis

The morphology of the synthetic samples obtained by thermal treatment of $\text{Bi}_2\text{O}_2\text{CO}_3$ precursor at different temperature was observed by SEM. As shown in Fig. 4A, the flower-like $\text{Bi}_2\text{O}_2\text{CO}_3$ microspheres, which are composed of numerous nanosheets ($\sim 15 \text{ nm}$ thickness) and approximately $6 \mu\text{m}$ in diameter, were successfully prepared using a citric acid assisted hydrothermal process. After thermal treatment at 290 °C, the morphology of the as-obtained sample is still flower-like structures, but some nanosheets are broken and disordered pores were formed (Fig. 4B). As the temperature increased to 330 °C, nanosheets were almost destroyed yet large number of nanocrystals were produced, which constitute the sample and retaining the flower-like structure (Fig. 4C). When the temperature was higher than 400 °C, all of the nanocrystals aggregated to form larger particles and ultimately forming coral-like structures (Fig. 4D). These results suggest that the $\text{Bi}_2\text{O}_2\text{CO}_3$ nanosheets are gradually transformed to $\beta\text{-Bi}_2\text{O}_3$ and $\alpha\text{-Bi}_2\text{O}_3$ nanocrystals after heat treatment, but the overall flower-like microsphere structures remain unchanged. Therefore, the $\text{Bi}_2\text{O}_2\text{CO}_3$ precursors are act as self-sacrifice template in this process.

The detailed structural information of the sample synthesized after calcination at 290 °C ($\beta\text{-Bi}_2\text{O}_3/\text{Bi}_2\text{O}_2\text{CO}_3$ composites) was further studied by TEM and high-resolution TEM (HRTEM) analysis. The TEM image (Fig. 5A) reveals that the sample had a diameter of $\sim 6 \mu\text{m}$ with microsphere-like appearance, which is in good agreement with the size and shape of SEM observed. And these flower-microspheres are composed of numerous nanosheets (Fig. 5B). Higher magnification TEM images (Fig. 5C) provide the detailed morphology of the as-obtained sample, revealing that many nanocrystals with size $\sim 15 \text{ nm}$ are homogeneously dispersed and embedded in the two dimensional nanosheets matrix, forming a sesame-biscuit-like structure. The typical HRTEM image, as shown in Fig. 5D, further demonstrates the detailed nano-junction structure. It clearly shows two different lattice images with d -spacings of 0.32 and 0.27 nm, which correspond to the (201) lattice plane of $\beta\text{-Bi}_2\text{O}_3$ and the (110) lattice plane of $\text{Bi}_2\text{O}_2\text{CO}_3$, respectively. These results indicate that a heterojunction was constructed between $\beta\text{-Bi}_2\text{O}_3$ (nanocrystals) and $\text{Bi}_2\text{O}_2\text{CO}_3$ (nanosheets) with large contact surfaces in the as-synthesized composites.

3.1.3. Surface area analysis

The specific surface area and porosity of the as-synthesized samples were investigated by nitrogen adsorption and desorption. As shown in Fig. 6, all of the isotherms of the samples including the $\text{Bi}_2\text{O}_2\text{CO}_3$ precursor, $\beta\text{-Bi}_2\text{O}_3/\text{Bi}_2\text{O}_2\text{CO}_3$ composites, and pure $\beta\text{-Bi}_2\text{O}_3$ correspond to type IV with a H3 hysteresis loop, which suggests mesoporous features [45]. In comparison to the apparent area of the $\text{Bi}_2\text{O}_2\text{CO}_3$ microspheres ($18.1 \text{ m}^2 \text{ g}^{-1}$), the BET surface area of the calcined samples was smaller ($12.5 \text{ m}^2 \text{ g}^{-1}$ for 300 °C and $7.4 \text{ m}^2 \text{ g}^{-1}$ for 330 °C sample). In addition, the corresponding pore

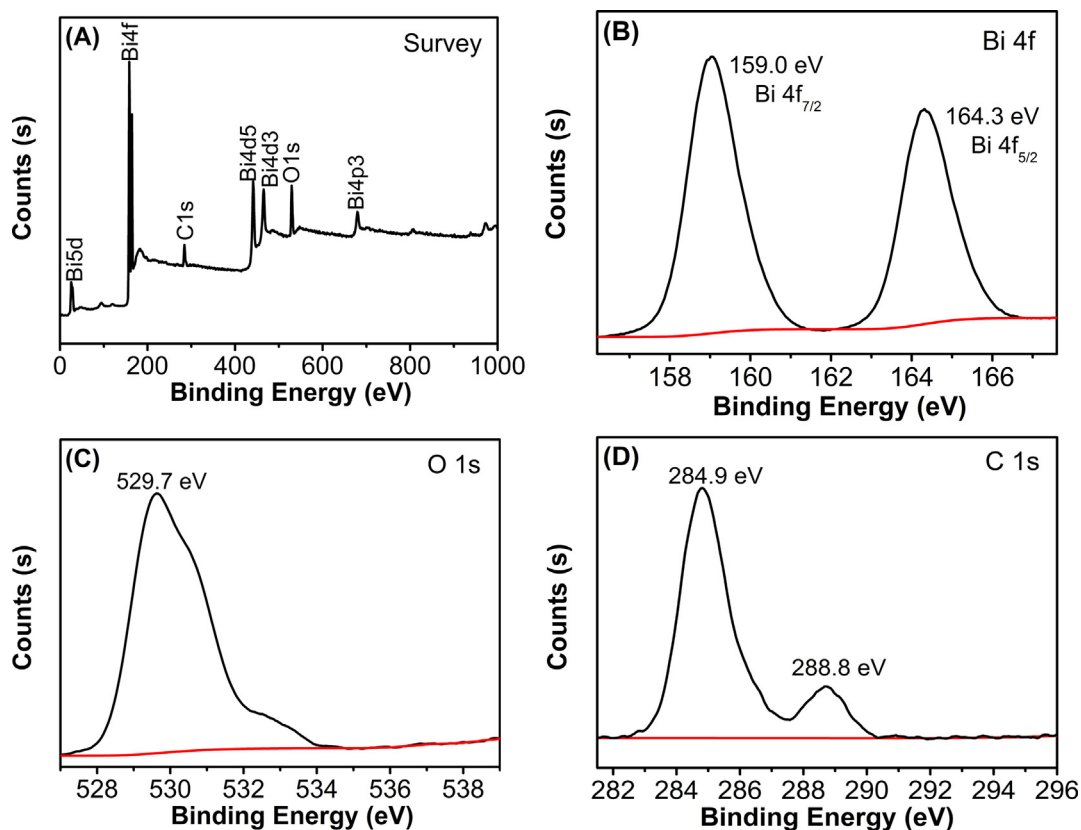


Fig. 3. XPS spectra of β - $\text{Bi}_2\text{O}_3/\text{Bi}_2\text{O}_2\text{CO}_3$ obtained after calcination at 290°C (A) survey spectrum and high-resolution core spectrum for (B) Bi 4f, (C) O 1s, and (D) C 1s.

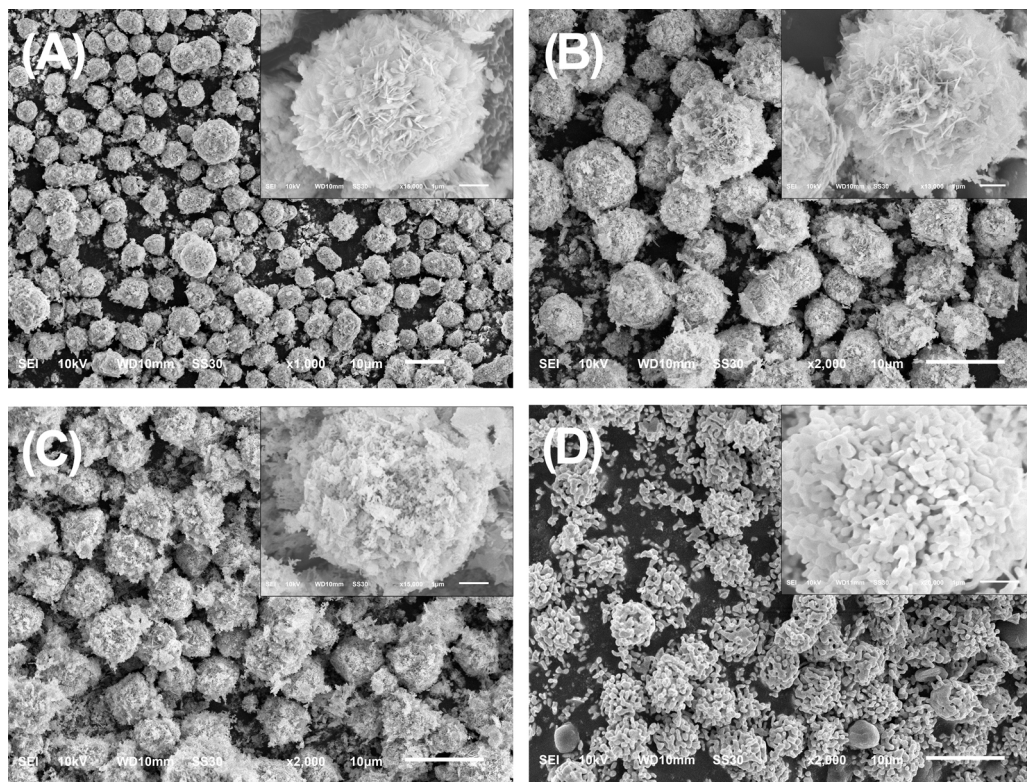


Fig. 4. SEM images of the as-synthesized samples: (A) Prior to calcination and (B)–(D) after calcination at 290°C , 330°C , and 400°C , respectively. The inset shows a high magnification SEM image of the corresponding sample.

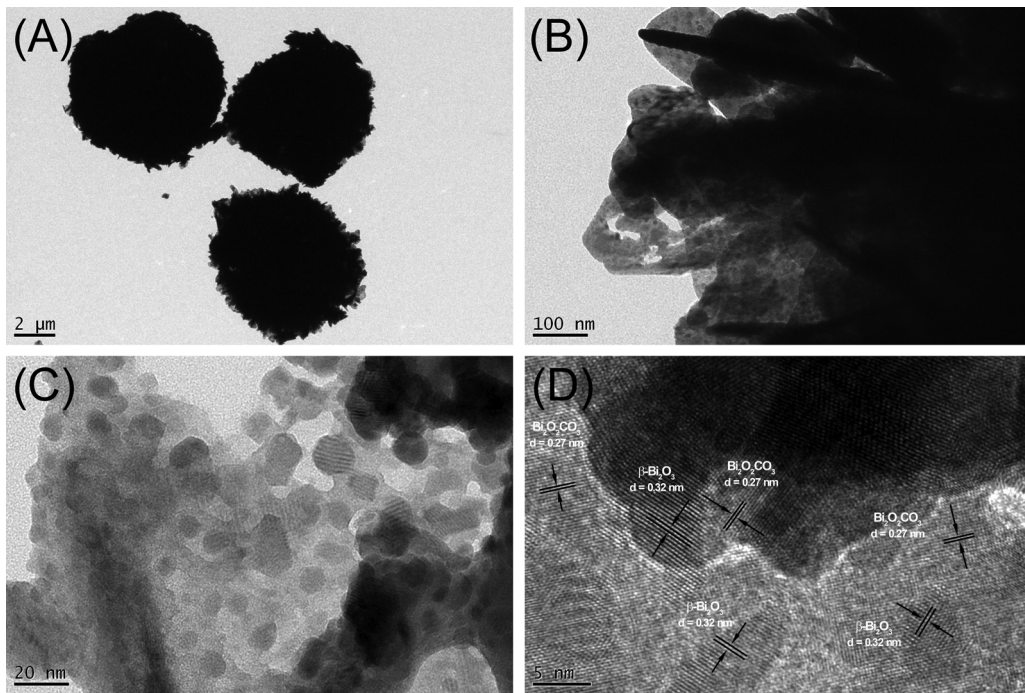


Fig. 5. TEM and HRTEM images of the as-synthesized sample calcined at 290 °C.

size distributions of $\text{Bi}_2\text{O}_2\text{CO}_3$, $\beta\text{-Bi}_2\text{O}_3/\text{Bi}_2\text{O}_2\text{CO}_3$ and $\beta\text{-Bi}_2\text{O}_3$, which were determined using the BJH method (inset in Fig. 6), indicated that the average mesoporous diameters were 12.9, 10.3 and 5.8 nm, respectively, with broad distributions. The mesoporous features, which possess broadly distributed pores, most likely arise from their inter-nanosheet/nanocrystals spacing [46]. The reduction of the specific surface area and porous diameters after heat treatment were due to the growth in the particle size after calcination at a higher temperature.

3.1.4. Photoabsorption and energy band structures

Fig. 7 shows the DRS of the as-synthesized samples. The maximal absorbance wavelengths of $\text{Bi}_2\text{O}_2\text{CO}_3$ (calcined at 250 °C), $\beta\text{-Bi}_2\text{O}_3/\text{Bi}_2\text{O}_2\text{CO}_3$ (calcined at 300 °C) and $\beta\text{-Bi}_2\text{O}_3$ (calcined at 330 °C) are approximately 367, 540, and 554 nm, respectively. Correspondingly, the materials displayed different colors ranging from beige white to brilliant yellow (inset of Fig. 7). Their band gap

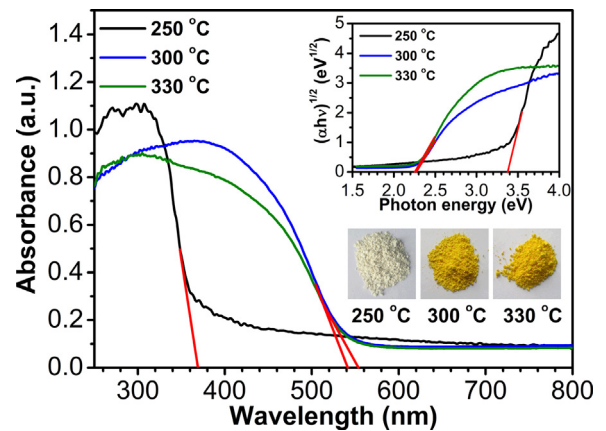


Fig. 7. UV-vis diffuse reflection spectra of the samples calcined at 250 °C ($\text{Bi}_2\text{O}_2\text{CO}_3$), 300 °C ($\beta\text{-Bi}_2\text{O}_3/\text{Bi}_2\text{O}_2\text{CO}_3$ composite), and 330 °C (pure $\beta\text{-Bi}_2\text{O}_3$). The inset shows the plots of $(\alpha h\nu)^{1/2}$ as a function of photon energy ($h\nu$) and photos of the samples.

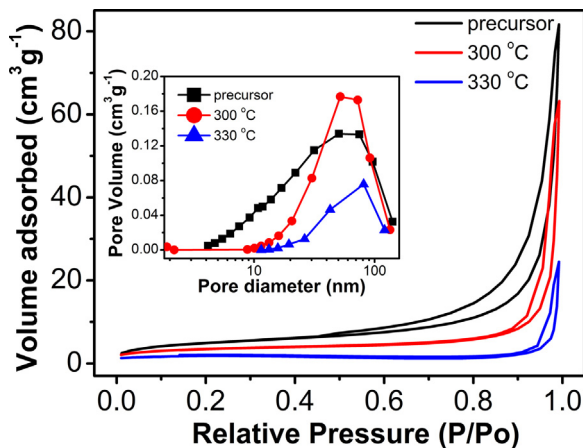


Fig. 6. Nitrogen adsorption-desorption isotherms and the corresponding pore-size distribution curves (inset) of the $\text{Bi}_2\text{O}_2\text{CO}_3$ precursor, $\beta\text{-Bi}_2\text{O}_3/\text{Bi}_2\text{O}_2\text{CO}_3$ composite calcined at 300 °C, and pure $\beta\text{-Bi}_2\text{O}_3$ obtained by calcination at 330 °C.

energy (E_g) was evaluated using the following equation (Eq. (7)) [47]:

$$\alpha(h\nu) = A(h\nu - E_g)^{n/2} \quad (7)$$

where α , ν , E_g , and A are the absorption coefficient, light frequency, band gap energy, and a constant, respectively, and n is determined by the type of optical transition in the semiconductor. According to the literature [48], the band gap energies (E_g values) of these samples were estimated from a plot of $(\alpha h\nu)^{1/2}$ as a function of the photon energy ($h\nu$) (inset of Fig. 7) to be approximately 3.38, 2.27, and 2.25 eV for $\text{Bi}_2\text{O}_2\text{CO}_3$, $\beta\text{-Bi}_2\text{O}_3/\text{Bi}_2\text{O}_2\text{CO}_3$, and $\beta\text{-Bi}_2\text{O}_3$, respectively. The values for $\text{Bi}_2\text{O}_2\text{CO}_3$ and $\beta\text{-Bi}_2\text{O}_3$ determined in this work are close to the values reported in the literatures [22,49].

The band positions of the as-synthesized $\beta\text{-Bi}_2\text{O}_3$ and $\text{Bi}_2\text{O}_2\text{CO}_3$ were calculated using the following empirical equation: (Eq. (8)) [50]

$$E_{\text{VB}} = X - E^e + 0.5 E_g \quad (8)$$

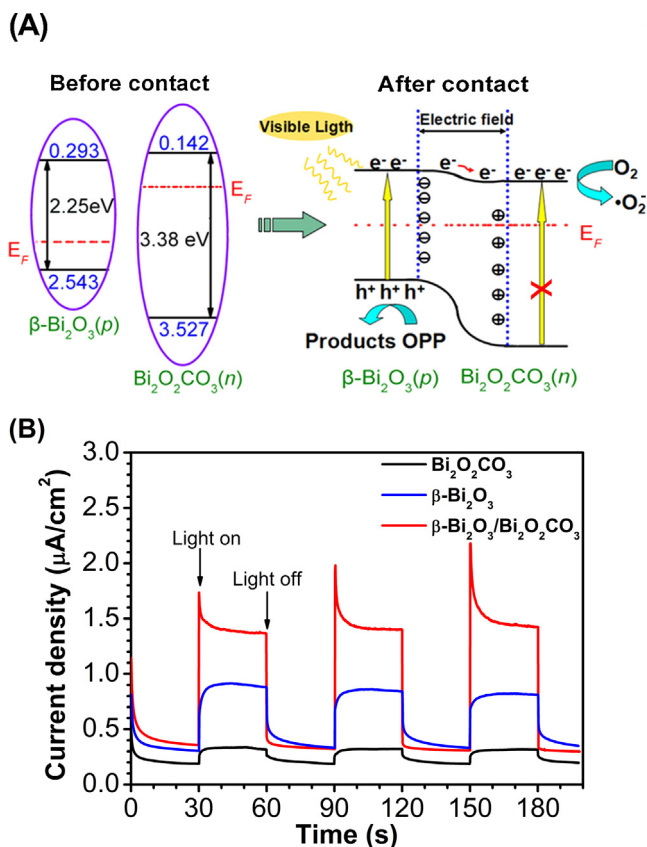


Fig. 8. (A) Schematic diagram of separation of electron-hole pairs over $\beta\text{-Bi}_2\text{O}_3/\text{Bi}_2\text{O}_2\text{CO}_3$ p-n junction under visible-light irradiation. (B) Photocurrent transient responses for $\text{Bi}_2\text{O}_2\text{CO}_3$, $\beta\text{-Bi}_2\text{O}_3$, and $\beta\text{-Bi}_2\text{O}_3/\text{Bi}_2\text{O}_2\text{CO}_3$ composites (calcined at 300 °C).

where E_{VB} is the valence band edge potentials, X is the electronegativity of the semiconductor, which is the geometric mean of the electronegativity of the constituent atoms, E^e is the energy of the free electrons on the hydrogen scale (approximately 4.5 eV), E_g is the band gap energy of the semiconductor, and E_{CB} (conductance band edge potentials) can be determined by $E_{CB} = E_{VB} - E_g$. The results are shown in Fig. 8A, and a nested band structure for single $\beta\text{-Bi}_2\text{O}_3$ and $\text{Bi}_2\text{O}_2\text{CO}_3$ was observed. These band structures seem unfavorable for the separation of photoinduced carriers. However, in the $\beta\text{-Bi}_2\text{O}_3/\text{Bi}_2\text{O}_2\text{CO}_3$ composites, $\beta\text{-Bi}_2\text{O}_3$ is a p-type semiconductor while $\text{Bi}_2\text{O}_2\text{CO}_3$ is an n-type semiconductor [40]. Therefore, after their contact with each other, the $\beta\text{-Bi}_2\text{O}_3/\text{Bi}_2\text{O}_2\text{CO}_3$ p-n junction will be formed when their Fermi levels (E_F) reached equilibrium state, and a newly formed energy band structure is formed in the interactive structure. As shown in Fig. 8A, it is clearly shown that only $\beta\text{-Bi}_2\text{O}_3$ can be activated due to its low band gap energy when the $\beta\text{-Bi}_2\text{O}_3/\text{Bi}_2\text{O}_2\text{CO}_3$ composite is exposed to visible-light irradiation. And then the reformed energy band structure was favorable for the fast separation of electrons from $\beta\text{-Bi}_2\text{O}_3$ to $\text{Bi}_2\text{O}_2\text{CO}_3$ due to the effect of inner electric field, analogous to other kinds of p-n junctions [51,37]. Therefore, the composites are predicted to exhibit better photocatalytic performance than the single phase.

To gain more insight into the high separation efficiency of photo-induced charges in the hybrid $\beta\text{-Bi}_2\text{O}_3/\text{Bi}_2\text{O}_2\text{CO}_3$, photocurrents were measured for the $\text{Bi}_2\text{O}_2\text{CO}_3$, $\beta\text{-Bi}_2\text{O}_3$, $\beta\text{-Bi}_2\text{O}_3/\text{Bi}_2\text{O}_2\text{CO}_3$ electrodes, as shown in Fig. 8B. It can be seen that fast photocurrent responses via on-off cycles were observed in these electrodes under visible-light irradiation, which may directly correlate with the separation efficiency of photogenerated carriers.

The results show that the photocurrent of $\text{Bi}_2\text{O}_2\text{CO}_3$ is rather low under visible light ascribed to its large band gap (3.38 eV), while $\beta\text{-Bi}_2\text{O}_3/\text{Bi}_2\text{O}_2\text{CO}_3$ electrodes is significantly higher than that of single $\beta\text{-Bi}_2\text{O}_3$, clearly indicating that the heterojunction results in more effective separation of electron-hole pairs [52]. Consequently, the formation of $\beta\text{-Bi}_2\text{O}_3/\text{Bi}_2\text{O}_2\text{CO}_3$ p-n heterojunctions largely reduced the recombination rate of the photogenerated electrons and holes thus may result in higher photodegradation performance.

3.2. Photocatalytic degradation of OPP

3.2.1. Evaluation of photocatalytic activity

The photocatalytic degradation of OPP over the samples annealed at different temperatures was evaluated under visible-light irradiation. As shown in Fig. 9A, the heat treatment temperatures had a significant influence on the photocatalytic activity. The sample calcined at 300 °C ($\beta\text{-Bi}_2\text{O}_3/\text{Bi}_2\text{O}_2\text{CO}_3$ composites) exhibited the best activity, and the pure $\beta\text{-Bi}_2\text{O}_3$ (annealed at 330 °C) and mixed $\beta\text{-Bi}_2\text{O}_3/\alpha\text{-Bi}_2\text{O}_3$ samples (annealed at 350 °C) exhibited the second and third best positions, while the pure $\alpha\text{-Bi}_2\text{O}_3$ (annealed at 400 or 500 °C) and $\text{Bi}_2\text{O}_2\text{CO}_3$ (annealed at 250 °C) samples exhibited poor performances. The low photocatalytic activity for $\beta\text{-Bi}_2\text{O}_3/\text{Bi}_2\text{O}_2\text{CO}_3$ sample calcined at 280 °C may be attributed to it contains only a very small amount of $\beta\text{-Bi}_2\text{O}_3$ (Fig. 1B), while $\text{Bi}_2\text{O}_2\text{CO}_3$ is not able to activate under visible-light illumination.

Then, the best performance sample, i.e. $\beta\text{-Bi}_2\text{O}_3/\text{Bi}_2\text{O}_2\text{CO}_3$ composites calcined at 300 °C, was compared to that of N-doped TiO_2 (synthesized according to a previously published procedure [53]), commercial $\beta\text{-Bi}_2\text{O}_3$, and a mechanical mixture containing 95% pure $\beta\text{-Bi}_2\text{O}_3$ and 5% pure $\text{Bi}_2\text{O}_2\text{CO}_3$, as shown in Fig. 9B. Under identical irradiation for 45 min, only 7.1% degradation of OPP was observed using the N-doped TiO_2 as a photocatalyst, and a degradation of 61.4% was observed using the commercial $\beta\text{-Bi}_2\text{O}_3$. In addition, the mechanical mixture resulted in a degradation of 90.0%, while an OPP removal ratio of 99.8% was obtained over the as-synthesized $\beta\text{-Bi}_2\text{O}_3/\text{Bi}_2\text{O}_2\text{CO}_3$ composites.

The degradation kinetics of OPP using these samples was also investigated by fitting the experimental data to the Langmuir–Hinshelwood model [54]. Because the reactant concentration is low, the following pseudo first-order kinetics equation (Eq. (9)) was used:

$$-\ln\left(\frac{C_t}{C_0}\right) = k_{\text{app}}t \quad (9)$$

where C_0 and C_t are the reactant concentrations at times $t=0$ and $t=t$, respectively, and k_{app} (min^{-1}) is the apparent reaction rate constant determined by plotting $\ln(C_0/C_t)$ as a function of the reaction time (t). The results indicate that the reaction kinetics of all of the samples can be fitted to the pseudo first-order rate model with high correlation coefficients ($R > 0.95$), as shown in Fig. 9C and D. The k_{app} values are calculated to be 0.000156, 0.000943, 0.129, 0.0655, 0.0401, 0.0104, 0.00384, 0.0016, 0.0218, and 0.0503 min^{-1} for samples annealed at 250, 280, 300, 330, 350, 400, and 500 °C as well as N-doped TiO_2 , commercial $\beta\text{-Bi}_2\text{O}_3$, and mechanical mixture of $\beta\text{-Bi}_2\text{O}_3$ with $\text{Bi}_2\text{O}_2\text{CO}_3$, respectively, which indicated that the reaction rate constant of the $\beta\text{-Bi}_2\text{O}_3/\text{Bi}_2\text{O}_2\text{CO}_3$ composites was approximately 2, 2.6, 6, 13, 80, and 827 times higher than that of the as-synthesized $\beta\text{-Bi}_2\text{O}_3$, $\beta\text{-Bi}_2\text{O}_3$ mixture with $\text{Bi}_2\text{O}_2\text{CO}_3$, commercial $\beta\text{-Bi}_2\text{O}_3$, as-synthesized $\alpha\text{-Bi}_2\text{O}_3$, N-doped TiO_2 , and as-synthesized $\text{Bi}_2\text{O}_2\text{CO}_3$, respectively. These results demonstrate that the as-synthesized $\beta\text{-Bi}_2\text{O}_3/\text{Bi}_2\text{O}_2\text{CO}_3$ flower-like microspheres have excellent visible light-induced activity for the degradation of OPP. The superior photoreactivity of the $\beta\text{-Bi}_2\text{O}_3/\text{Bi}_2\text{O}_2\text{CO}_3$ photocatalyst can thus be ascribed to p-n heterojunctions formed between $\beta\text{-Bi}_2\text{O}_3$ and

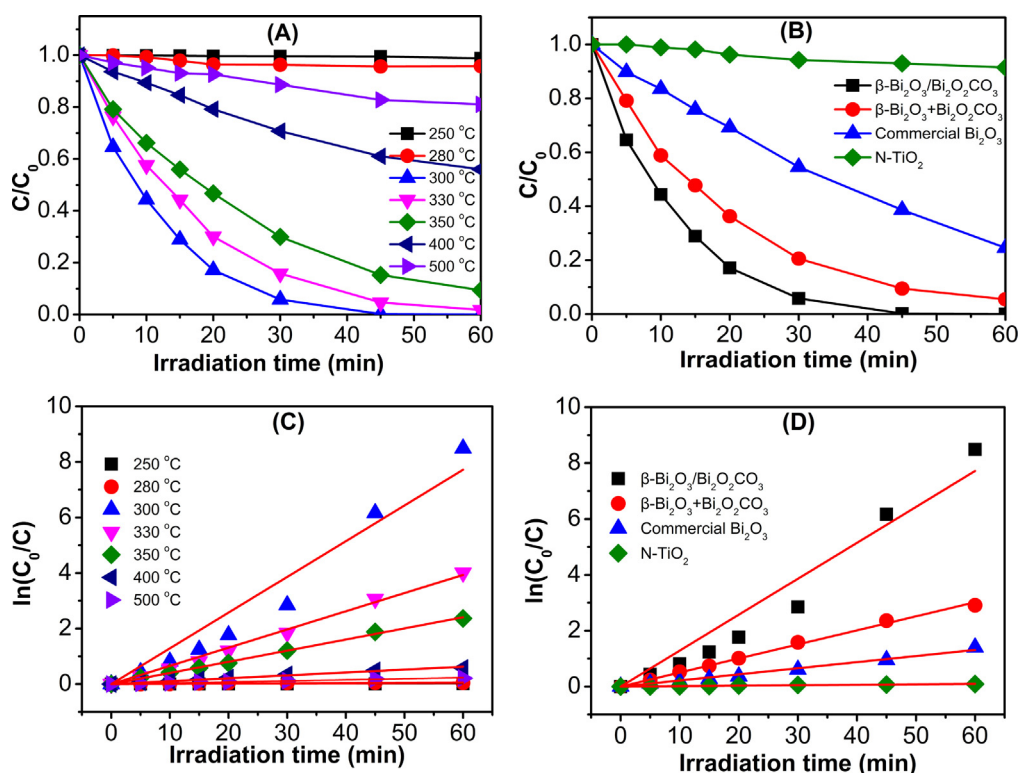


Fig. 9. (A) Photocatalytic degradation kinetics of OPP over the samples calcined at different temperatures. (B) Photocatalytic degradation kinetics of OPP over N-doped TiO₂, commercial β -Bi₂O₃, physical mixture of β -Bi₂O₃ and Bi₂O₂CO₃, and the β -Bi₂O₃/Bi₂O₂CO₃ composite calcined at 300 °C. (C) and (D) Linear plots of $\ln(C_0/C_t)$ as a function of degradation time.

Bi₂O₂CO₃ with large junction interface, favorable band gap energy, relatively high specific surface areas, and flower-like hierarchical micro/nano structures.

3.2.2. Effects of process parameters

Different initial concentrations of the OPP solutions (ranging from 10 to 50 mg L⁻¹) and varied as-synthesized β -Bi₂O₃/Bi₂O₂CO₃ doses (from 0.2 to 2.0 g L⁻¹) were employed to study the effects of the operating conditions on the photocatalytic system. As shown in Fig. 10A, lower OPP concentrations degrade more efficiently because as the initial concentration of OPP increases, additional organic molecules can be absorbed on the surface of the photocatalyst reducing the photogeneration of the reactive oxygen species due to over loading of the active sites. In addition, an increase in the OPP concentration leads to an increase in the amount of incident photons that may be intercepted by the pollutant molecules before they reach the catalyst [55].

The effect of the catalyst dose on the degradation efficiency is shown in Fig. 10B. The photodegradation efficiency of OPP increased when the concentration of the β -Bi₂O₃/Bi₂O₂CO₃ micro-flowers increased from 0.2 to 1.0 g L⁻¹, but the enhancement was not significant when the concentration exceeded 1.0 g L⁻¹. Obviously, lower catalytic activity was observed when a smaller amount of catalyst was used because less catalytic active sites were available. However, if the dosage is too high, an increase in the opacity and light scattering of the catalyst and a decrease in the number of catalytic surface active sites will occur, which is likely caused by aggregation of the catalyst particles [56] and which will result in no longer enhanced degradation efficiency.

3.2.3. Evaluation of mineralization

Effective mineralization of contaminants throughout the photocatalytic process requires prevention of secondary pollution in practical applications. The total organic carbon (TOC) was selected

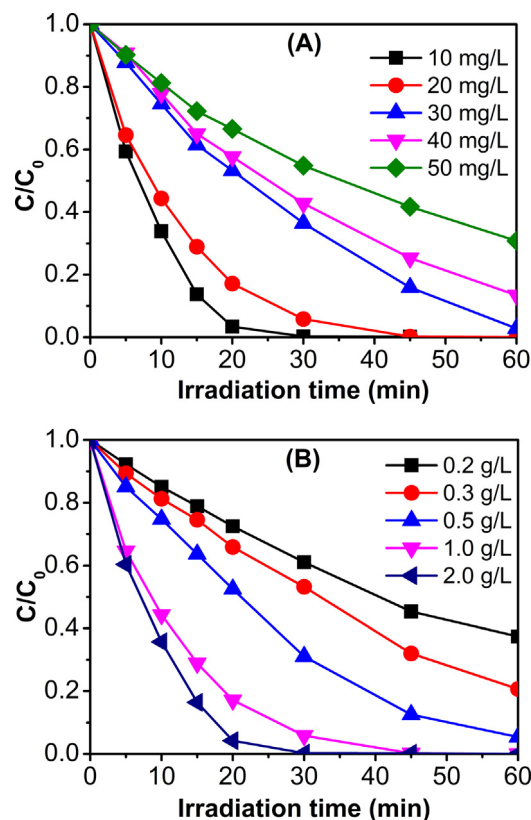


Fig. 10. Effects of (A) the initial concentration of OPP and (B) the catalyst dose on the photocatalytic activity of the β -Bi₂O₃/Bi₂O₂CO₃ micro-flowers. Experimental conditions: catalyst dose is 1 g L⁻¹ for the OPP concentration experiments and C₀ = 20 mg L⁻¹ for the experiments using varied catalyst doses.

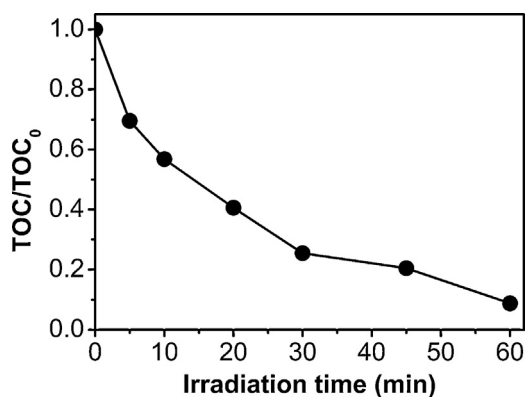


Fig. 11. TOC removal of OPP over the as-synthesized β - $\text{Bi}_2\text{O}_3/\text{Bi}_2\text{O}_2\text{CO}_3$ micro-flowers under visible-light irradiation.

as a mineralization index for this system. As shown in Fig. 11, the TOC decreased as the photoreaction time increased. After irradiation for 60 min, 91.2% of the TOC was eliminated, indicating that the OPP was effectively mineralized by the as-synthesized β - $\text{Bi}_2\text{O}_3/\text{Bi}_2\text{O}_2\text{CO}_3$ micro-flowers under visible-light irradiation.

3.2.4. Degradation intermediates and photocatalytic mechanism

After photocatalytic reaction for 10 min, a sample solution was extracted, concentrated, and analyzed by GC–MS to identify the degradation intermediates of OPP. As shown in Fig. 12A, the results indicate that in addition to OPP (retention time = 21.1 min), ethyl phenethyl ether (retention time = 8.6 min), phenyl acetaldehyde (retention time = 8.9 min), and phenylacetic acid (retention time = 9.5 min) were observed as intermediates.

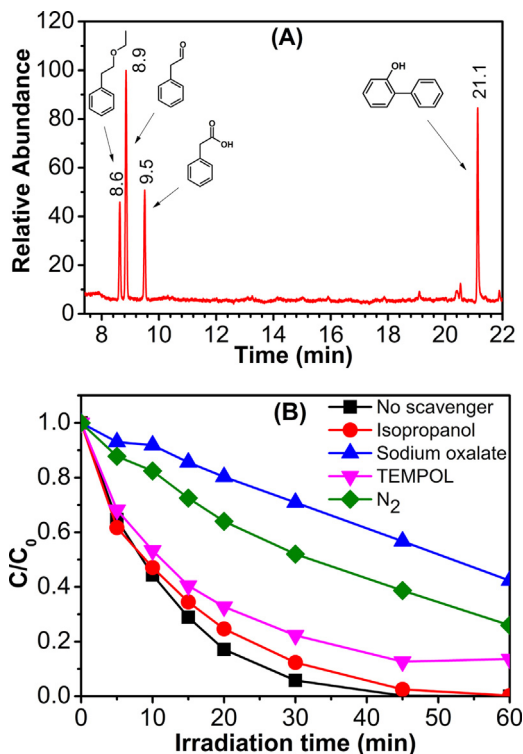


Fig. 12. (A) GC–MS chromatogram of the reaction solution after photocatalytic degradation for 10 min. (B) Photodegradation performances with different scavengers: no scavenger, 50 mmol L^{-1} isopropanol, 0.1 mmol L^{-1} sodium oxalate, 0.05 mmol L^{-1} TEMPOL, and N_2 in the photodegradation of OPP over the as-synthesized β - $\text{Bi}_2\text{O}_3/\text{Bi}_2\text{O}_2\text{CO}_3$ micro-flowers.

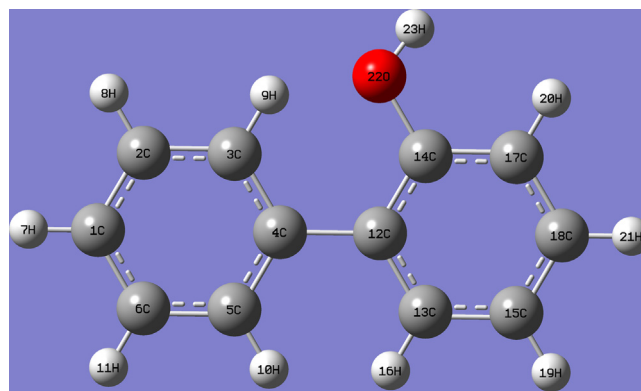


Fig. 13. The molecular structure of OPP with atoms labeled.

To evaluate the role of the primary reactive species, scavenger experiments were performed by adding individual scavengers to the photodegradation system. Isopropanol was used to remove $\bullet\text{OH}$ that diffused into the solution bulk, sodium oxalate was used to remove h^+ bound to the surface, 4-hydroxy-2,2,6,6-tetramethylpiperidinyloxy (TEMPOL) was used to remove $\bullet\text{O}_2^-$, and N_2 was used to remove oxygen that dissolved in the solution bulk [57,58]. As shown in Fig. 12B, the addition of isopropanol did not change the photodegradation efficiency compared to the absence of a scavenger, indicating the $\bullet\text{OH}$ does not play an important role in this system. However, inhibition of the photocatalytic performance was observed when sodium oxalate was used to quench h^+ , which confirmed the importance of h^+ in this oxidation process. In addition, in the presence of TEMPOL and N_2 , the removal ratio of OPP decreased, which suggested that $\bullet\text{O}_2^-$ or dissolved oxygen may play a role in the reaction.

To further understand the photoreaction intermediates of the system, a theoretical calculation of the frontier electron density of OPP was carried out, and the result is shown in Fig. 13 and Table 1. According to the frontier molecular orbital theory, for a radical reaction, the point of attack occurs at the position where the highest density of the sum of each electron occurs when they are in the highest occupied molecular orbital (HOMO) and lowest unoccupied molecular orbital (LUMO) [59], while for the direct hole oxidation, the first reaction site is predicted on the basis of $2\text{FED}_{\text{HOMO}}^2$ value [60]. In this study, the highest $2\text{FED}_{\text{HOMO}}^2$ value of OPP is found at the C_1 , C_4 , C_{12} , and C_{14} atoms (Table 1). Therefore, these C atoms should be the active sites from which an electron is extracted by holes, resulting in ring breakdown, and subsequently producing other oxidation products by further oxidized. The detection of phenethyl products may be explained by after attacked C_{12} and C_{14} atoms, while other intermediates not to be observed may be

Table 1
The frontier electron density and atom point charge of OPP.

Atom label	$2\text{FED}_{\text{HOMO}}^2$	$\text{FED}_{\text{HOMO}} + \text{FED}_{\text{LUMO}}$
C_1	0.152	0.222
C_2	0.030	0.063
C_3	0.105	0.175
C_4	0.155	0.234
C_5	0.098	0.324
C_6	0.029	0.024
C_{12}	0.141	0.295
C_{13}	0.058	0.269
C_{14}	0.142	0.372
C_{15}	0.041	0.099
C_{17}	0.016	0.153
C_{18}	0.115	0.354
O_{22}	0.052	0.066

ascribed to their short survival time and the limiting of the current experimental conditions.

In combination with the analysis of intermediates and the experiments of reactive oxygen species, the OPP photodegradation over the as-synthesized β - $\text{Bi}_2\text{O}_3/\text{Bi}_2\text{O}_2\text{CO}_3$ micro-flowers may be dominated by the direct hole and $\bullet\text{O}_2^-$ radicals oxidation, which leads to ring cleavage and mineralize rather than oxidation by $\bullet\text{OH}$ as previously reported [8]. Therefore, the degradation by-products do not contain a large quantity of hazardous substances, such as multi-hydroxybiphenyls or hydroquinone/quinones, and a high mineralization level can be achieved due to improvement in the oxidation process, which is important for effective treatment of OPP containing wastewaters.

4. Conclusions

Novel flower-like β - $\text{Bi}_2\text{O}_3/\text{Bi}_2\text{O}_2\text{CO}_3$ composite microspheres assembled with nanosheets were successfully synthesized via a facile hydrothermal-calcining process. The XRD, SEM, TEM, and DSC results of the samples obtained under different calcination temperatures indicated that the $\text{Bi}_2\text{O}_2\text{CO}_3$ precursor acted as a self-sacrificing morphology template for the products. In comparison to the pure β - Bi_2O_3 , α - Bi_2O_3 , and $\text{Bi}_2\text{O}_2\text{CO}_3$ samples, the as-synthesized β - $\text{Bi}_2\text{O}_3/\text{Bi}_2\text{O}_2\text{CO}_3$ nanocomposites exhibited enhanced photocatalytic activity for the degradation of OPP under visible-light irradiation. The superior photoreactivity of the composite photocatalyst may be due to the formation of p–n junction with effectively separation of electrons and holes, favorable band gap energy, relatively high specific surface areas, and hierarchical micro/nano structures. In addition, the photocatalytic mechanism studies indicated that the photogenerated hole and $\bullet\text{O}_2^-$ radicals are the main reactive species in this visible-light photocatalytic system, which resulted in a high mineralization efficiency for OPP.

Acknowledgements

This work was financially supported by the National Natural Science Foundation of China (No. 21477040), the Natural Science Foundation of Guangdong Province of China (No. S2012040007074), and the Scientific Research Foundation of Graduate School of South China Normal University (2013kyjj050).

References

- [1] K.E. Appel, Arch. Toxicol. 74 (2000) 61–71.
- [2] J.P. Voets, P. Pipyn, P. Van Lancker, W. Verstraete, J. Appl. Microbiol. 40 (1976) 67–72.
- [3] T. Sembiring, J. Winter, Appl. Microbiol. Biotechnol. 31 (1989) 89–92.
- [4] Y. Seki, M. Ogawa, Bull. Chem. Soc. Jpn. 83 (2010) 712–715.
- [5] M. Gmurek, M. Olak-Kucharczyk, J.S. Miller, S. Ledakowicz, Inżynieria i Aparatura Chemiczna 51 (2012) 119–122.
- [6] M. Olak-Kucharczyk, J.S. Miller, S. Ledakowicz, Ozone: Sci. Eng. 34 (2012) 300–305.
- [7] A. Kubacka, M. Fernandez-Garcia, G. Colon, Chem. Rev. 112 (2011) 1555–1614.
- [8] A.A. Khodja, T. Sehili, J.F. Pilichowski, P. Boule, J. Photochem. Photobiol. A: Chem. 141 (2001) 231–239.
- [9] M. Pelaez, N.T. Nolan, S.C. Pillai, M.K. Seery, P. Falaras, A.G. Kontos, P.S. Dunlop, J.W. Hamilton, J.A. Byrne, K. O'Shea, Appl. Catal. B: Environ. 125 (2012) 331–349.
- [10] X. Xiao, C. Liu, R. Hu, X. Zuo, J. Nan, L. Li, L. Wang, J. Mater. Chem. 22 (2012) 22840–22843.
- [11] A. Kudo, K. Omori, H. Kato, J. Am. Chem. Soc. 121 (1999) 11459–11467.
- [12] M. Shang, W. Wang, H. Xu, Cryst. Growth Des. 9 (2008) 991–996.
- [13] C. Guo, J. Xu, S. Wang, L. Li, Y. Zhang, X. Li, CrystEngComm 14 (2012) 3602–3608.
- [14] F. Dong, W. Ho, S.C. Lee, Z. Wu, M. Fu, S. Zou, Y. Huang, J. Mater. Chem. 21 (2011) 12428–12436.
- [15] H. Cheng, B. Huang, J. Lu, Z. Wang, B. Xu, X. Qin, X. Zhang, Y. Dai, Phys. Chem. Chem. Phys. 12 (2010) 15468–15475.
- [16] L. Zhang, W. Wang, L. Zhou, H. Xu, Small 3 (2007) 1618–1625.
- [17] L. Zhou, W. Wang, H. Xu, S. Sun, M. Shang, Chem. Eur. J. 15 (2009) 1776–1782.
- [18] F. Zheng, G. Li, Y. Ou, Z. Wang, C. Su, Y. Tong, Chem. Commun. 46 (2010) 5021–5023.
- [19] H. Lu, S. Wang, L. Zhao, B. Dong, Z. Xu, J. Li, RSC Adv. 2 (2012) 3374–3378.
- [20] L. Zhang, W. Wang, J. Yang, Z. Chen, W. Zhang, L. Zhou, S. Liu, Appl. Catal. A: Gen. 308 (2006) 105–110.
- [21] Y. Qiu, M. Yang, H. Fan, Y. Zuo, Y. Shao, Y. Xu, X. Yang, S. Yang, CrystEngComm 13 (2011) 1843–1850.
- [22] X. Xiao, R. Hu, C. Liu, C. Xing, C. Qian, X. Zuo, J. Nan, L. Wang, Appl. Catal. B: Environ. 140–141 (2013) 433–443.
- [23] D. Li, Y. Zhang, X. Zhou, S. Guo, J. Hazard. Mater. 258 (2013) 42–49.
- [24] Y. Xu, Z. Zhang, W. Zhang, Mater. Res. Bull. 48 (2013) 1420–1427.
- [25] C. Wang, C. Shao, Y. Liu, L. Zhang, Scr. Mater. 59 (2008) 332–335.
- [26] M. Gui, W. Zhang, Q. Su, C. Chen, J. Solid State Chem. 184 (2011) 1977–1982.
- [27] K. Vignesh, R. Priyanka, M. Rajarajan, A. Suganthi, Mater. Sci. Eng.: B 178 (2013) 149–157.
- [28] S. Park, J. Jun, H.W. Kim, C. Lee, Solid State Commun. 149 (2009) 315–318.
- [29] F. Dong, S.C. Lee, Z. Wu, Y. Huang, M. Fu, W. Ho, S. Zou, B. Wang, J. Hazard. Mater. 195 (2011) 346–354.
- [30] M. HoáSo, Chem. Commun. 21 (2006) 2265–2267.
- [31] Y. Zheng, F. Duan, M. Chen, Y. Xie, J. Mol. Catal. A: Chem. 317 (2010) 34–40.
- [32] W. Wang, H. Cheng, B. Huang, X. Lin, X. Qin, X. Zhang, Y. Dai, J. Colloid Interface Sci. 402 (2013) 34–39.
- [33] X. Huang, H. Chen, Appl. Surf. Sci. 284 (2013) 843–848.
- [34] H. Gan, G. Zhang, H. Huang, J. Hazard. Mater. 250 (2013) 131–137.
- [35] G. Zhu, M. Hojamberdiev, K. Katsumata, X. Cai, N. Matsushita, K. Okada, P. Liu, J. Zhou, Mater. Chem. Phys. 142 (2013) 95–105.
- [36] K.H. Reddy, S. Martha, K.M. Parida, Inorg. Chem. 52 (2013) 6390–6401.
- [37] J. Cao, X. Li, H. Lin, S. Chen, X. Fu, J. Hazard. Mater. 239 (2012) 316–324.
- [38] G. Nagaraju, Y. Hwan Ko, J. Su Yu, Mater. Lett. 116 (2014) 64–67.
- [39] H. Jiang, H. Endo, H. Natori, M. Nagai, K. Kobayashi, Mater. Res. Bull. 44 (2009) 700–706.
- [40] G. Cai, L. Xu, B. Wei, J. Che, H. Gao, W. Sun, Mater. Lett. 120 (2014) 1–4.
- [41] X. Xiao, W. Zhang, RSC Adv. 1 (2011) 1099–1105.
- [42] S. Shamaila, A.K.L. Sajjad, F. Chen, J. Zhang, Appl. Catal. B: Environ. 94 (2010) 272–280.
- [43] Y. Schuhl, H. Baussart, R. Delobel, M. Le Bras, J. Leroy, L. Gengembre, J. Grimbolt, J. Chem. Soc., Faraday Trans. 1: Phys. Chem. Cond. Phases 79 (1983) 2055–2069.
- [44] F. Dong, H. Wang, G. Sen, Z. Wu, S.C. Lee, J. Hazard. Mater. 187 (2011) 509–516.
- [45] K. Sing, D.H. Everett, R. Haul, L. Moscou, R.A. Pierotti, J. Rouquerol, T. Siemieniowska, Pure Appl. Chem. 57 (1985) 603–619.
- [46] J. Zhang, F. Shi, J. Lin, D. Chen, J. Gao, Z. Huang, X. Ding, C. Tang, Chem. Mater. 20 (2008) 2937–2941.
- [47] X. Zhang, Z.H. Ai, F.L. Jia, L.Z. Zhang, J. Phys. Chem. C 112 (2008) 747–753.
- [48] F. Qin, G. Li, R. Wang, J. Wu, H. Sun, R. Chen, Chem. Eur. J. 18 (2012) 16491–16497.
- [49] T. Zhao, J. Zai, M. Xu, Q. Zou, Y. Su, K. Wang, X. Qian, CrystEngComm 13 (2011) 4010–4017.
- [50] Y. Xu, M.A.A. Schoonen, Am. Mineral. 85 (2000) 543–556.
- [51] G. Dai, J. Yu, G. Liu, J. Phys. Chem. C 115 (2011) 7339–7346.
- [52] F. Dong, Z. Zhao, T. Xiong, Z. Ni, W. Zhang, Y. Sun, W. Ho, ACS Appl. Mater. Interfaces 5 (2013) 11392–11401.
- [53] G. Yang, Z. Jiang, H. Shi, T. Xiao, Z. Yan, J. Mater. Chem. 20 (2010) 5301–5309.
- [54] J. Xu, W. Meng, Y. Zhang, L. Li, C. Guo, Appl. Catal. B: Environ. 107 (2011) 355–362.
- [55] I.K. Konstantinou, T.A. Albanis, Appl. Catal. B: Environ. 49 (2004) 1–14.
- [56] M.A. Gondal, X.F. Chang, Z.H. Yamani, Chem. Eng. J. 165 (2010) 250–257.
- [57] W. Wang, T.W. Ng, W.K. Ho, J. Huang, S. Liang, T. An, G. Li, J.C. Yu, P.K. Wong, Appl. Catal. B: Environ. 129 (2013) 482–490.
- [58] W. Wang, Y. Yu, T. An, G. Li, H.Y. Yip, J.C. Yu, P.K. Wong, Environ. Sci. Technol. 46 (2012) 4599–4606.
- [59] N. San, A. Hatipoğlu, G. Koçtürk, Z. Çınar, J. Photochem. Photobiol. A: Chem. 146 (2002) 189–197.
- [60] K. Fukui, T. Yonezawa, H. Shingu, J. Chem. Phys. 20 (1952) 722–725.